Engineering Analysis with Boundary Elements 166 (2024) 105769

Contents lists available at ScienceDirect

Engineering Analysis with Boundary Elements

journal homepage: www.elsevier.com/locate/enganabound

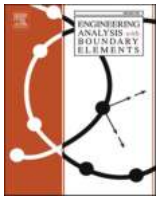

Protuberance placement mastery: Shock wave control integration with Coanda effect to thrust vectoring on a sonic jet

Mohammad Reza Soufivand [a], Mohammad Hojaji [b,*], Mohammad Hossein Razavi Dehkordi [b]

[a] Department of Mechanical Engineering, South Tehran Branch, Islamic Azad University, Tehran, Iran
[b] Department of Mechanical Engineering, Aerospace and Energy Conversion Research Center, Najafabad Branch, Islamic Azad University, Najafabad, Iran

ARTICLE INFO

Keywords:
Experimental aerodynamics
CFD
Compressible flow
Thrust vector control
Protuberance
Coanda effect

ABSTRACT

Thrust Vector Control (TVC) is a technique that allows precise control over the direction and velocity of an aerial vehicle. This paper presents a novel approach combining shock wave control and the Coanda effect to apply this technique in sonic flows. The objective is to achieve more eligible and operational control over the deviation angles of the thrust vector. The research is conducted through numerical simulations and experimental tests to investigate the impact of protuberance location (1, 3.5, and 5 mm), protuberance width (1.5, 2 mm), depth of penetration (2, 6, and 10%), and nozzle pressure ratio (ranging from 2.1 to 4) on the flow field, thrust vector angle, and thrust value of the nozzle. The system's behavior depends on the protuberance location, pressure ratio, and penetration depth. The location of the protuberance influences the shocks and flow separation from the Coanda flap. Increasing the penetration depth up to 10% enhances system stability and reduces the protuberance location's influence on flow deviation. The study highlights the significant effect of protuberance placement on thrust loss, with higher penetration depths resulting in a more significant decrease. The system's behavior in terms of flow deviation is more stable at specific penetration depths and pressure ratios. The results show that the proposed technique achieves a maximum deviation angle of 83° for a sonic jet. In addition, the findings contribute to understanding TVC using protuberances and the Coanda effect. The proposed technique offers advantages in simplicity, reliability, and control performance. It opens possibilities for efficient and maneuverable aerospace vehicles, with applications in UAVs, surveillance, and search and rescue missions.

1. Introduction

TVC is a mechanism that allows a vehicle to control its direction and velocity by directing the thrust generated by its engine. This mechanism operates by directing the thrust produced by the engine without changing the vehicle's aerodynamic shape. The thrust vector is critical during the initial phase of movement or launch when aerodynamic forces are negligible due to the lack of speed. TVC can also perform complex aerial maneuvers that would be impossible to be performed with traditional aircraft control systems. TVC provides increased maneuverability, stability, and precision control. Engineers can now design more maneuverable, precise, and stable vehicles than ever before, opening up new applications and capabilities. TVC has also helped develop reusable rockets, which are less expensive and more efficient than traditional ones. Researchers are also investigating the use of TVC in new applications, such as unmanned aerial vehicles (UAVs), where TVC could enable new capabilities and applications. UAVs outfitted with TVC could be used for surveillance, search and rescue missions, and various other missions. TVC has significantly impacted the aerospace industry, allowing for the development of high-performance aerospace vehicles. Despite the numerous advantages of TVC, its implementation needs to be improved. The system's complexity, which requires precise engineering to ensure that the vehicle remains stable and controllable, is one of the primary challenges TVC faces. Furthermore, implementing TVC can be prohibitively expensive, limiting its use to high-performance applications. TVC will undoubtedly play a critical role in enabling new capabilities and applications as aerospace technology evolves. As a result, while implementing TVC presents its own challenges, researchers are working to develop new technologies that make it more accessible and efficient [1-11]. Examples of these techniques are the use of multiple nozzles, moving nozzles, interference methods, secondary injection methods, and protuberances. Because exhaust gasses are scorching, it is imperative that controllers be fabricated from unique and resistant alloys when tabs and vanes are employed. Furthermore, the persistent presence of these controllers may

* Corresponding author.
E-mail address: hojaji_m@pmc.iaun.ac.ir (M. Hojaji).

https://doi.org/10.1016/j.enganabound.2024.105769
Received 13 February 2024; Received in revised form 25 April 2024; Accepted 5 May 2024
Available online 12 June 2024

Nomenclature

Latin abbreviations

t	Time (s)
u	x-velocity component (m/s)
v	y-velocity component (m/s)
P	Static pressure (bar)
P_0	Total nozzle pressure
NPR	Ratio of total pressure to ambient pressure (dimensionless)
F	Force (N)
D*	Throat diameter (mm)
H	Protuberance height (mm); Pen.

Greek abbreviations

ρ	Density (kg/m3)
μ	Dynamic viscosity of fluid (Pa.s)
γ	Ratio of specific heats
δ	Jet deviation angle (degree)
Θ	The angle of the pressure holes on the Coanda flap

Subscripts

x	Horizontal spatial coordinates
y	Vertical spatial coordinates
∞	Ambient

The use of secondary fluid injection to create a shock is one of the most common methods of fluid thrust vector control because the fluid injected in the sonic and supersonic flow acts like a solid body and causes shock formation and flow deviation. However, injecting fluid with a specific flow rate and direction in the flow necessitates special valves, connections, and mechanisms, which complicate the system and, because they transfer fluid at high pressure and temperature, wear out over time, increasing maintenance costs. A solid body is used to cause shock directly in the protuberance technique, which has no disadvantages as a newer method than the secondary injection method [15-18].

Another FTVC method that has received attention from researchers is using the Coanda effect of a secondary flow. Secondary flow, either suction [19-21], blowing [22-25], or both simultaneously [26], can effectively deflect the primary jet path. However, the application of secondary flow associated with the Coanda effect has been limited in supersonic flows [27,28] because supersonic Coanda flows are pretty complex, with shock structures, and are highly sensitive to nozzle and flap geometry. A unique TVC technique using auxiliary currents and taking advantage of the Coanda effect [29] is presented in a proposed patent plan, in which only simple shut-off valves are used, no mechanical or moving parts are used, and it can create suction. It also does not require any power to create suction and blow. Two studies on a similar nozzle were conducted in 2016 and 2018 [30,31], with the researchers achieving a significant deviation angle of 72° (Fig. 2).

While such extreme angles in the deviation of the thrust vector were successfully achieved by the researchers in these studies, they were attained only within a narrow range of low-pressure ratios. The more significant point lies in the lack of reasonable control over the thrust

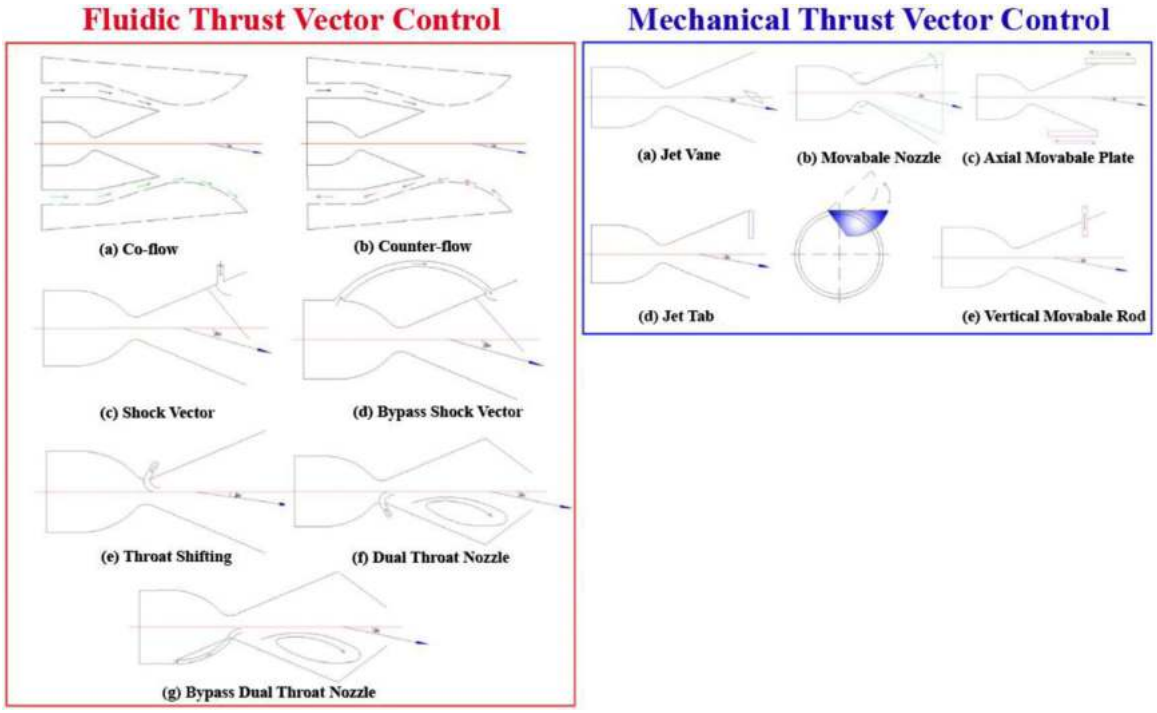

Fig. 1. A schematic of conventional thrust vector control; (A) FTVC & (B) MTVC [11].

lead to losses in the overall flow. Also, the critical control speed decreases as the number of mechanical parts increases in the method of moving nozzles. Fluid control systems are generally simpler than mechanical systems, which is a significant advantage [1,12]. According to one previous study, FTVC techniques can improve thrust capacity by 7–12% and operating costs by 37–53% [13]. In addition to the advantages they offer in nozzle cooling and stealth compared to conventional methods [14]. Fig. 1 depicts some of these methods' schematics.

vector. As depicted in Fig. 3, a sharp jump (approximately ten to sixty degrees) in the deviation of the thrust vector was encountered. Consequently, the system was rendered non-operational due to these flaws. In this study, the two techniques are combined by using the protuberance in the nozzle with the Coanda flaps and, as a new method, creating a more optimal and operational control in the deviation angles of the thrust vector in such a way that it takes advantage of the two techniques. It is also expected that, compared to bypass flows, such a design will

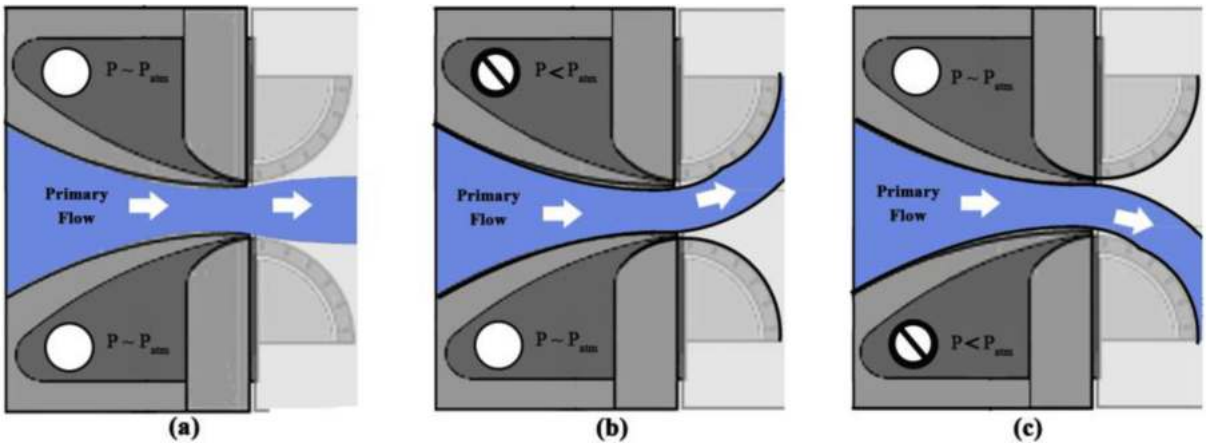

Fig. 2. Performance of discussed nozzle [31].

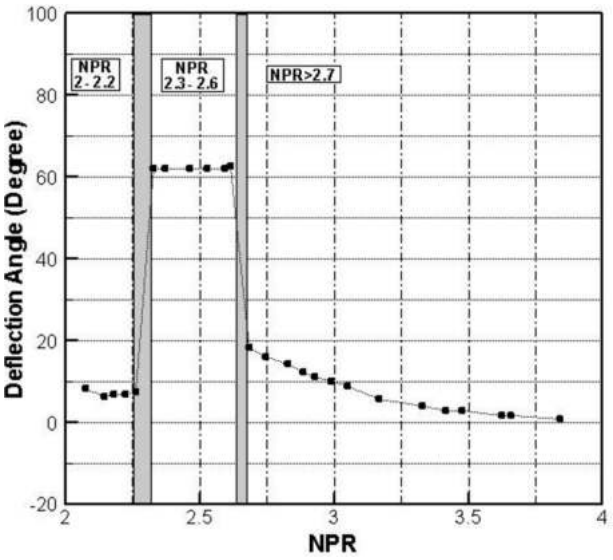

Fig. 3. Working range of discussed thrust vector technique [31].

result in a more significant deviation of the thrust vector (at higher pressure ratios). This study investigated the penetration depth of various protuberances (Pen. = 2, 6, and 10%) and their placement (Loc. = 1, 3.5, and 5 mm) with widths of 1.5 and 2 mm, across different nozzle total pressures (NPR = 2.1 to 4). It was determined to what extent these parameters would affect the flow field, thrust vector angle, and total amount of axial thrust of the nozzle. Various parameters, such as force values, jet deviation angle, pressure distribution on the surface of the Coanda, as well as density and Mach number contours, have been evaluated to quantitatively and qualitatively evaluate this technique. This research was generally done numerically, but experimental tests were also used to validate the results.

2. Experimental setup

In this investigation of thrust vector control (TVC) utilizing the Coanda effect, a convergent rectangular nozzle was designed and constructed with a length of 350 mm and a width of 250 mm. The nozzle's geometry closely resembled that of a previous study [31], except for the throat dimensions, which were set at 20 mm in width and 10 mm in height. Additionally, a protuberance was strategically placed within the nozzle's throat to induce deviation in the jet stream. The nozzle outlet featured quarter-circle flaps on both sides, each with a radius of 50 mm, and these were enclosed by two Plexiglas parts with a thickness of 10 mm. To investigate the pressure distribution on the Coanda surface, holes with diameters of 0.5 mm were drilled in the flaps. These holes were positioned every 5° of the flap to facilitate static pressure measurements. The schematics of the studied nozzle are depicted in Fig. 4, while the experimental setup of the nozzle is illustrated in Fig. 5.

An air compressor boasting a maximum pressure of 300 bars is employed to induce sonic flow within the nozzle. This compressor is connected to 24 air tanks, each with a capacity of 60 liters. The total pressure within the settling chamber remains constant throughout each experiment. A spherical valve and a pressure regulator regulate the pressure inside the settling chamber. The measurements encompass the axial and side components of the force, along with the pressure distribution on the Coanda flaps, conducted under various conditions.

The pressure holes on the Coanda surface have been connected to a sensor box to measure pressure distribution. This current investigation employs three types of Trafag sensors: −1 to 1, −1 to 4, and −1 to 10 bar gage. Additionally, a two-component force stand measures axial and side forces. This stand incorporates a four-bar mechanism and two Zemic L6D C3 load cells for force measurement. The nozzle is positioned above a metal frame, supported by four metal balls to minimize axial and lateral friction. The force stand features a 15 kgf force load cell in the axial direction and a 10 kgf load cell on the side. Calibration of the force stand is conducted using varied forces in the ranges of 0 to 7 kgf and at angles spanning from −80 to 80°.

The force components and measured pressure values are converted and transmitted to a computer through an Advantech USB-4711A card. The A/D card has a 12-bit resolution and a maximum sampling rate of 150 kS/s. Throughout the current study, all experiments were conducted with a data sampling frequency of 400 Hz. The schematic of the experimental setup is depicted in Fig. 6.

The measurement error of the pressure sensors falls within the range of 0.1%FS. Pressure measurement errors stem from sensor accuracy and data card inaccuracies, manifesting as an error bar in certain graphs presented subsequently. Furthermore, owing to the interplay of load cell errors and internal interference effects, the overall precision of the force stand is diminished compared to the individual load cell precision. Error sources within this system encompass load cell errors, A/D data card inaccuracies, and force stand calibration errors. The statistical uncertainty was determined to be 45.2 g for mass and 2.2° for force angle.

Due to friction at the junctions, force residual is critical in force measurement systems. To scrutinize the prepared stand in this context, the raw load cell voltages were measured after each experiment and subsequently juxtaposed with the initial system voltage devoid of loading. As depicted in Fig. 7, the constructed stand exhibits negligible residual effects and the fluctuations in load cell voltages fall within the error margin of the data card.

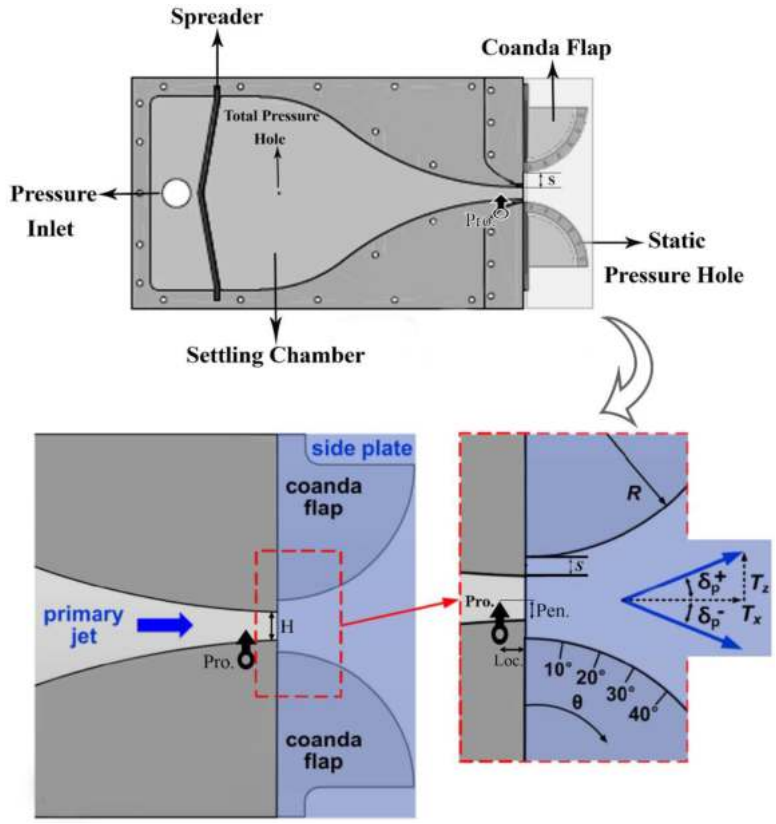

Fig. 4. Schematic of the system used in this research.

Fig. 5. Image of the nozzle experimental setup.

3. Governing equations and the numerical approach

A numerical simulation of the nozzle flow field in the presence of the Coanda effect was conducted. To achieve this, the 2D compressible steady form of the Reynolds-averaged Navier–Stokes (RANS) equations was discretized using a finite volume approach. The continuity, momentum, and energy conservation equations addressed this issue. The respective differential forms of these equations are presented below:

$$\frac{\partial(\rho u)}{\partial x}+\frac{\partial(\rho v)}{\partial y}=0 \tag{1}$$

$$\frac{\partial(\rho u^2)}{\rho x}+\frac{\partial(\rho uv)}{\partial y}=-\frac{\partial P}{\partial x} \tag{2}$$

$$\frac{\partial(\rho uv)}{\rho x}+\frac{\partial(\rho v^2)}{\partial y}=-\frac{\partial P}{\partial y} \tag{3}$$

$$\frac{\partial(uE)}{\partial x}+\frac{\partial(vE)}{\partial y}=-\frac{\partial(uP)}{\partial x}-\frac{\partial(vP)}{\partial y}-\frac{1}{Re.Pr}\left(\frac{\partial q_x}{\partial x}+\frac{\partial q_y}{\partial y}\right)+\frac{1}{Re}\left(\frac{\partial}{\partial x}\left(u\tau_{xx}+v\tau_{xy}\right)+\frac{\partial}{\partial y}\left(u\tau_{xy}+v\tau_{yy}\right)\right) \tag{4}$$

Here, t is time, x and y are space coordinates, p is pressure, ρ is density, and u and v are velocity components in the x and y directions, respectively [32]. The subscripts indicate derivatives with corresponding variables. The total energy per unit volume E is expressed as:

$$E=\frac{P}{\gamma-1}+\frac{1}{2}\rho\left(u^2+v^2\right) \tag{5}$$

where γ is the ratio of specific heats.

An implicit density-based algorithm was employed to solve the equations. The flux estimation type was determined using the Roe-averaged scheme, and initially, a first-order upwind scheme was

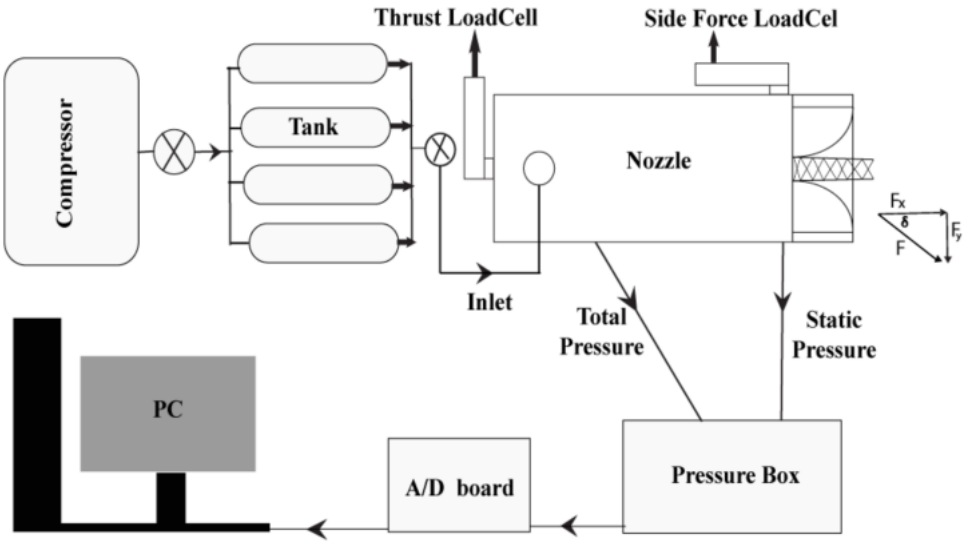

Fig. 6. Scheme of the experimental setup.

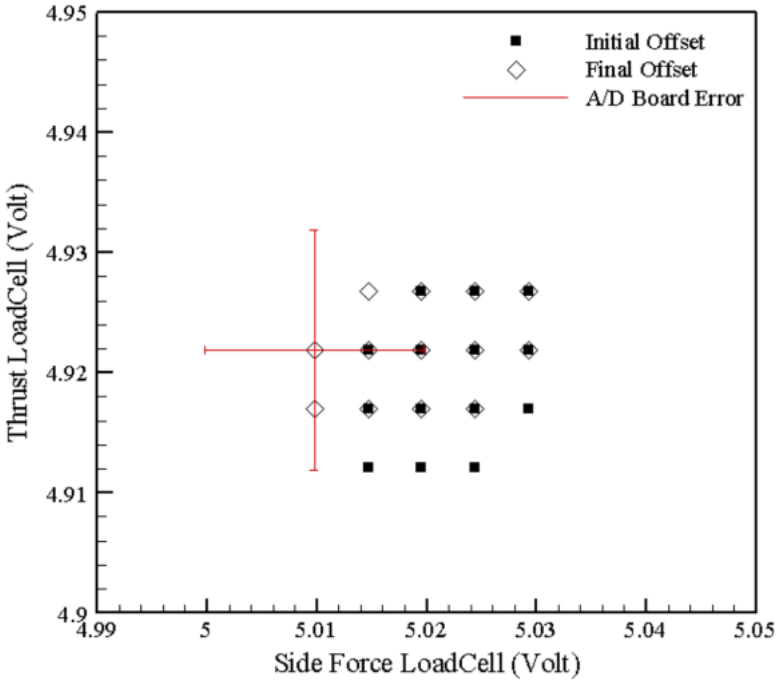

Fig. 7. Investigating the residual effects in force measurement system.

applied for spatial discretization until convergence behavior emerged. Subsequently, a second-order upwind scheme was adopted to enhance solution accuracy. The Courant-Friedrichs-Lewy (CFL) number commenced with a small value of 0.5 to ensure solution stability until convergence behavior manifested. Following convergence, the CFL number was increased to 2 to expedite the convergence process. Air (ideal gas) served as the working fluid throughout all the simulations.

The choice of turbulence model heavily influenced the accuracy of the solution. To comprehensively capture boundary layer separation, shock generation, and vortical regions, the k-ω SST turbulence model with curvature correction was utilized. The transport equations are as follows [33]:

$$\frac{\partial}{\partial x_i}(\rho k u_i) = \frac{\partial}{\partial x_j}\left(\Gamma_k \frac{\partial k}{\partial x_j}\right) + \widetilde{G}_k - Y_k + S_k \tag{6}$$

$$\frac{\partial}{\partial x_i}(\rho \omega u_i) = \frac{\partial}{\partial x_j}\left(\Gamma_\omega \frac{\partial \omega}{\partial x_j}\right) + G_\omega - Y_\omega + D_\omega + S_\omega \tag{7}$$

The equation under consideration encompasses several pivotal terms as outlined below: Turbulence kinetic energy (k) generation due to mean velocity gradients within the flow is denoted by $\widetilde{G_k}$. Similarly, G_ω encapsulates the generation of the specific dissipation rate (ω). Dissipation assumes a critical role, with Γ_k and Γ_ω delineating the dissipation of k and ω attributable to turbulence, respectively. The effective diffusivity of both k and ω are accounted for through the cross-diffusion term, denoted by D_ω. Finally, the contributions of viscous dissipation are represented by S_k and S_ω within the equation.

The deflection angle is calculated from the following equations [34]:

$$F_x = \int \{\rho u^2 + (P - P_\infty)\} dx \tag{8}$$

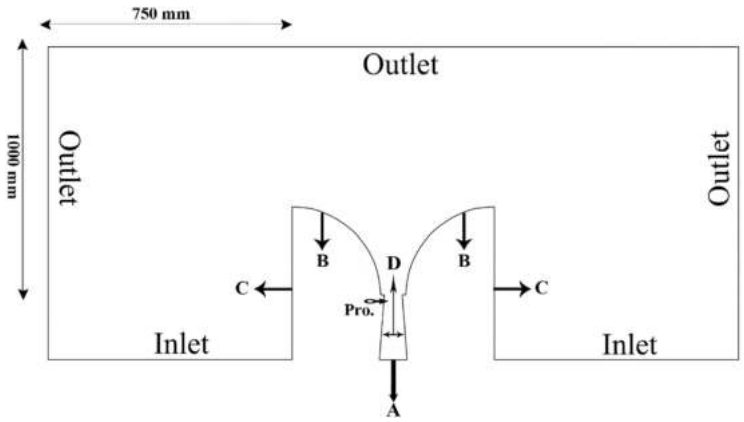

Fig. 8. Solution domain and boundary conditions.

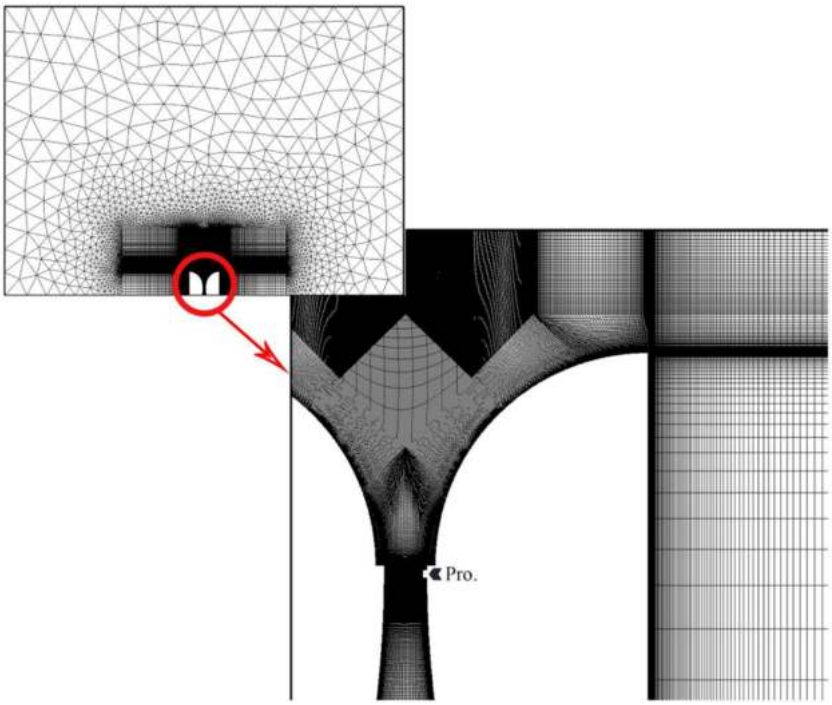

Fig. 9. Magnified structured grid in the solution domain.

Table 1
Grid Independence Analysis.

No.	Number of elements	Side force (N)	Thrust force (N)	Flow deflection angle (degree)
a	54,000	9.086	44.336	11.61
b	210,000	45.288	19.171	67.09
c	554,000	45.016	19.542	66.57

$$F_y = \int (\rho uv) dy \tag{9}$$

$$\delta = \frac{180}{\pi} tan^{-1} \frac{F_y}{F_x} \tag{10}$$

where Fx is the x-component of force, Fy is the y-component of force, and δ is the deflection angle.

3.1. Geometrical properties and boundary conditions

A rectangular sonic nozzle expels the jet into the atmosphere in the present investigation. The computational domain's length and width were set at 100 and 75 times that of the nozzle throat, respectively. A depiction of the domain and boundary conditions is presented in Fig. 8. To achieve varying NPR values, air at different pressures and a temperature of 300 K was introduced into the nozzle (NPR = 2.1 to 4) through the pressure inlet boundary (boundary A). On the outlet boundaries, a static pressure of 0.84 bar was imposed, accompanied by

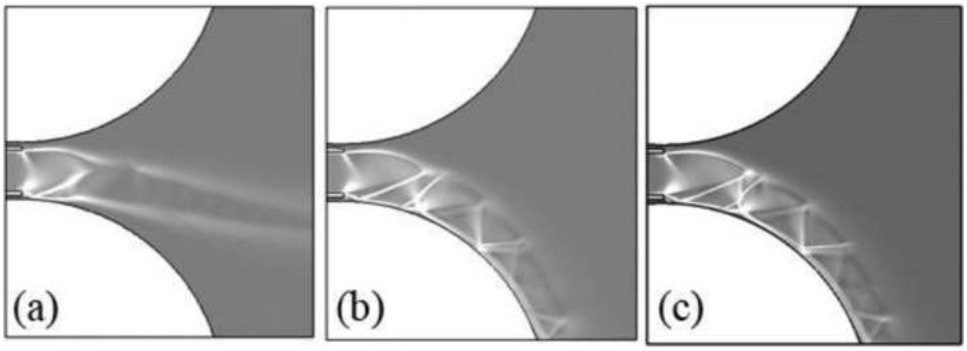

Fig. 10. Contour of density changes in three (a) coarse; (b) medium and (c) fine grids.

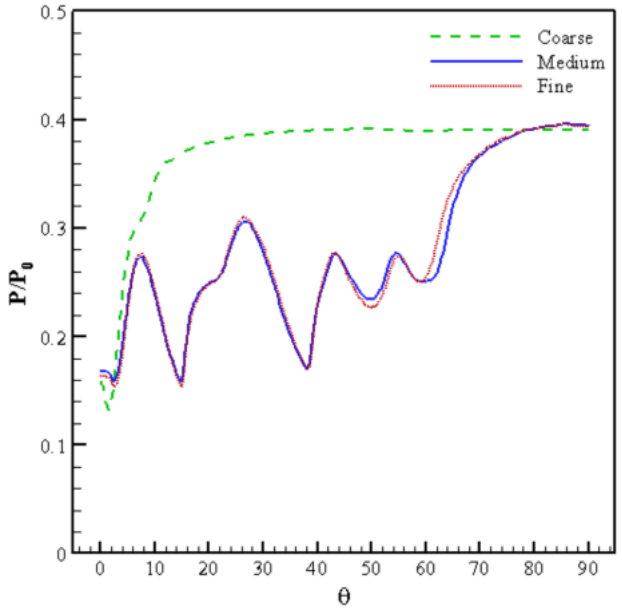

Fig. 11. Comparison of pressure distribution on Coanda surface for grids with different numbers of elements (NPR=2.5).

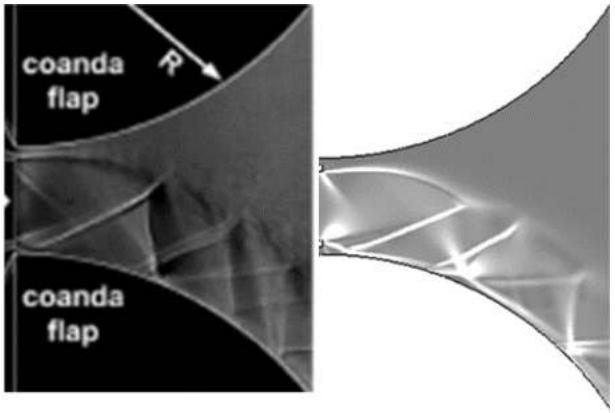

Fig. 12. Comparison of numerical simulation results and experimental shadowgraphs [31] at NPR=2.6 ($R_{Coanda\ Flap}$=50 mm, S = 2 mm).

an air temperature of 300 K. The boundaries encompass the nozzle wall and the surrounding environment where the jet discharges (boundaries B, C, and D).

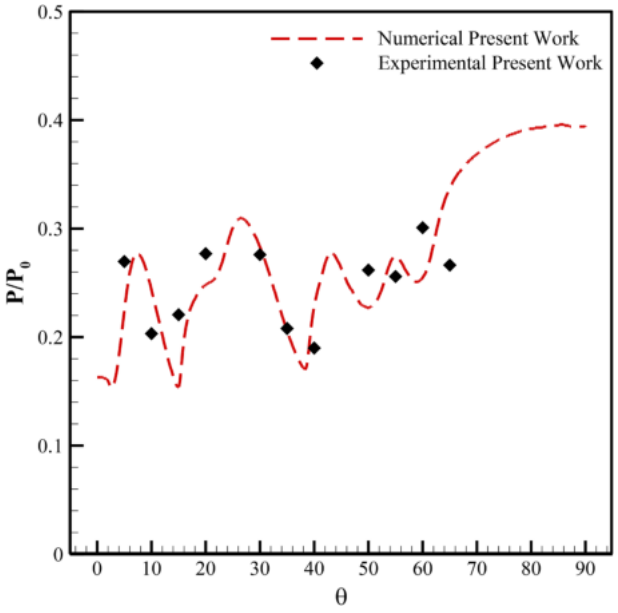

Fig. 13. Comparison of numerical and experimental pressure distributions on the Coanda flap NPR=2.5 ($R_{Coanda\ Flap}$=50 mm, S = 2 mm).

3.2. Grid independence analysis

A hybrid grid has been implemented in the computational domain, necessitating its division into two distinct parts for grid generation. Due to the intricate physics inherent in this problem, a structured grid has been employed for the internal segment and in proximity to the jet outlet. Simultaneously, the second part is an unstructured grid encompassing regions distant from the nozzle outlet. To ensure optimal skewness values, the grid for the structured part was meticulously designed, rendering its elements nearly perpendicular to the Coanda surfaces and boundaries (with a maximum skewness of 0.75% and a minimum orthogonality of 0.38%). Research in this domain indicates that failure to employ this method leads to a significant escalation in computational effort and numerical errors (refer to Fig. 9). To accurately simulate the laminar viscous sublayer, the grid size diminishes near the wall, yielding $y+$ values of less than one on the nozzle walls and Coanda surface.

Three different grids with varying element sizes were investigated for grid study. Table 1 and Fig. 10 show the simulation results. Accordingly, the flow in the coarse grid does not attach to the Coanda surface, indicating a calculation error.

The Fig. 11 illustrates the pressure distribution on the Coanda surface across three distinct grid sizes. A comparison of the results between medium and fine grid sizes reveals a negligible difference. Consequently,

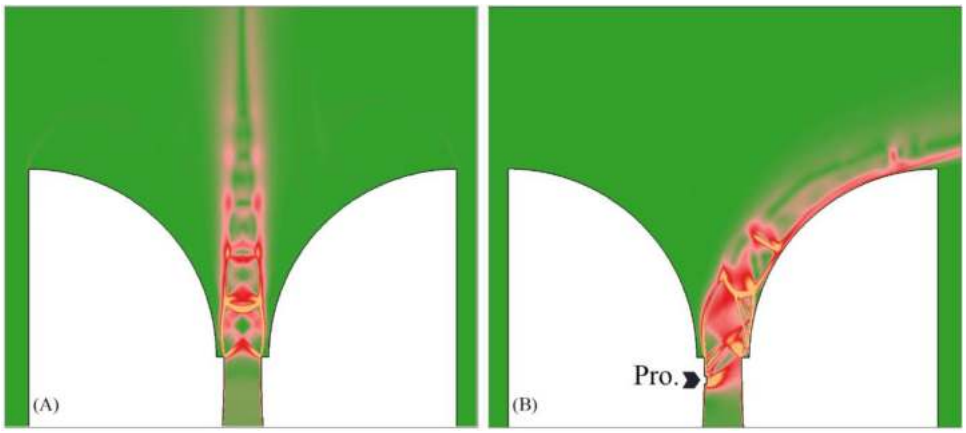

Fig. 14. The effect of the presence of a protuberance in the flow path of a sonic jet (NPR=2.5 - R = 50 mm - S = 2 mm); (A) Without protuberance & (B) With protuberance.

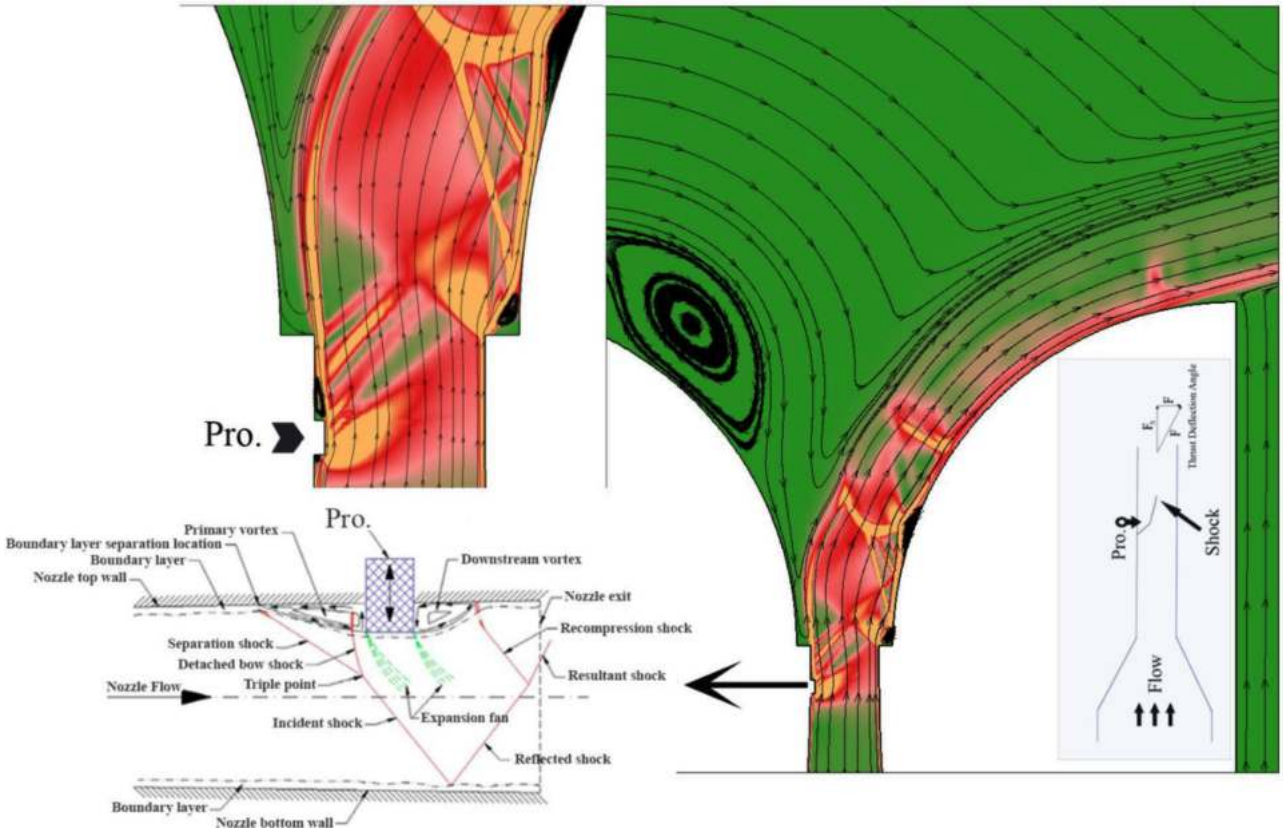

Fig. 15. Physics of the flow caused by the Coanda effect and the presence of a protuberance in the flow of a sonic jet (Loc.=5 mm, Pen.=0.6 mm, NPR=2.5) [11].

the medium grid, comprising 210,000 elements, was employed for the subsequent simulations.

3.3. Evaluation and validation

According to Fig. 12, the numerical simulation results align well with the experimental findings outlined in the reference [31] affirming the numerical methodology's credibility and accuracy.

The Fig. 13 illustrates the location and strength of shocks formed on the Coanda surface. The horizontal axis in this figure presents the Coanda flap angle, while the vertical axis depicts a dimensionless static pressure distribution based on total nozzle pressure. Generally, the results of numerical simulation and experimental tests closely align with each other, and any minor disparities in the location and strength of the shocks are attributed to numerical simulation errors and the uncertainties inherent in experimental testing.

4. Result and discussion

In this study, an evaluation has been conducted on the control performance of a sonic jet utilizing a protuberance and harnessing the Coanda effect. Various parameters have been considered, such as force values, jet deflection angles, pressure distribution on the Coanda flap, and contours depicting density variations and Mach numbers. The accuracy of the obtained results has been verified through experimental work. At the same time, numerical simulations have been employed to

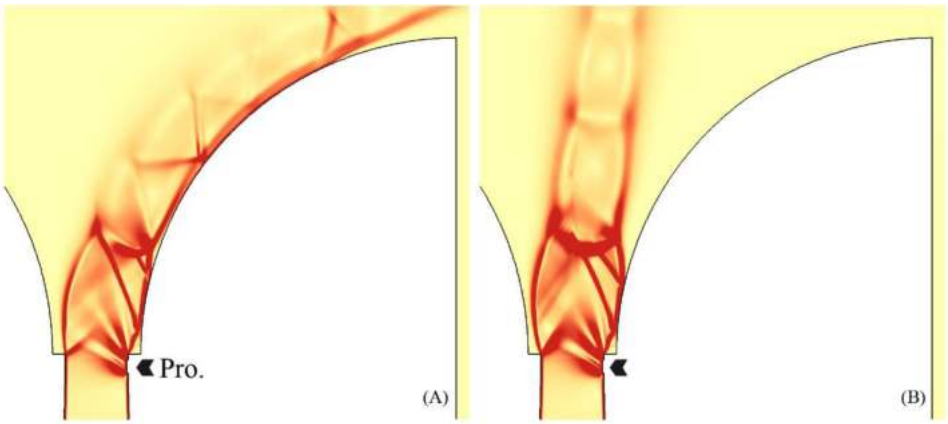

Fig. 16. The effect of NPR on flow physics (Loc.=1 mm, Pen. =2%), NPR; (A) 2.5 & (B) 3.

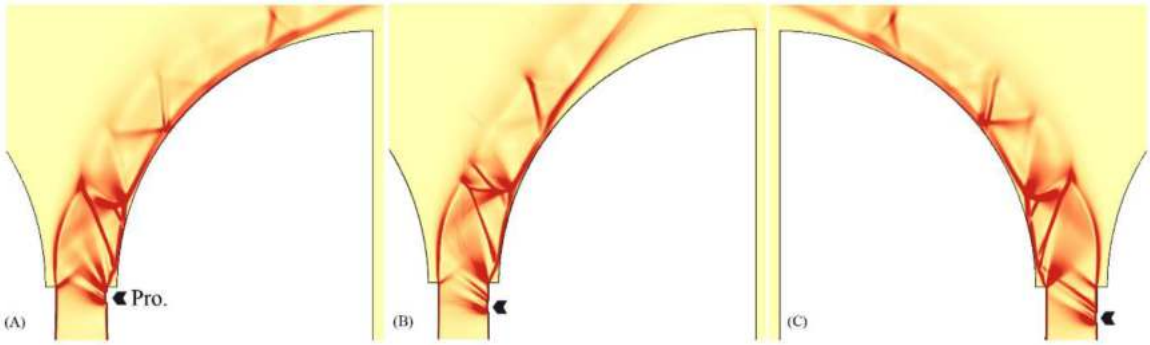

Fig. 17. Contour of density changes for the Pen. of 2% at NPR=2.5, Loc.; (A) 1 mm & (B) 3.5 mm & (C) 5 mm.

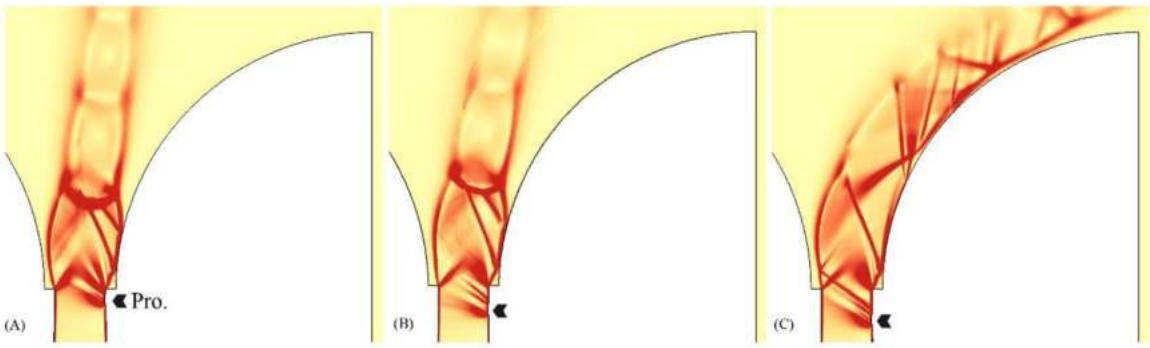

Fig. 18. Contour of density changes for the Pen. of 2% at NPR=3, Loc.; (A) 1 mm & (B) 3.5 mm & (C) 5 mm.

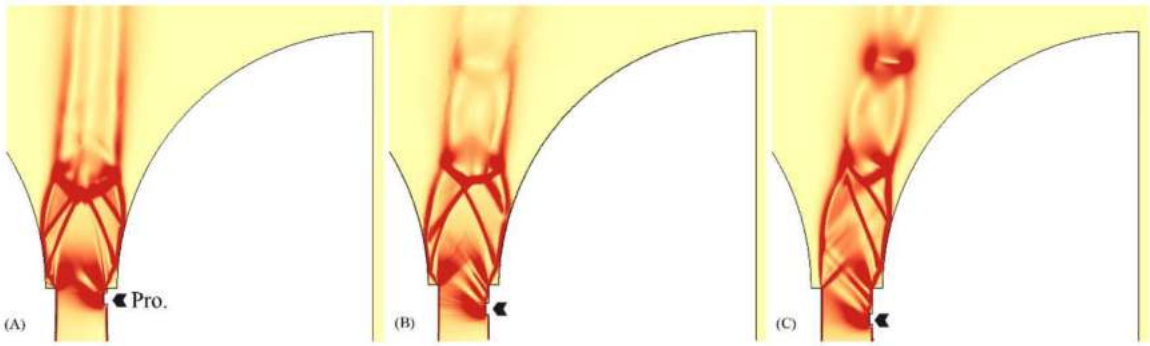

Fig. 19. Contour of density changes for the Pen. of 6% at NPR=3.5, Loc.; (A) 1 mm & (B) 3.5 mm & (C) 5 mm.

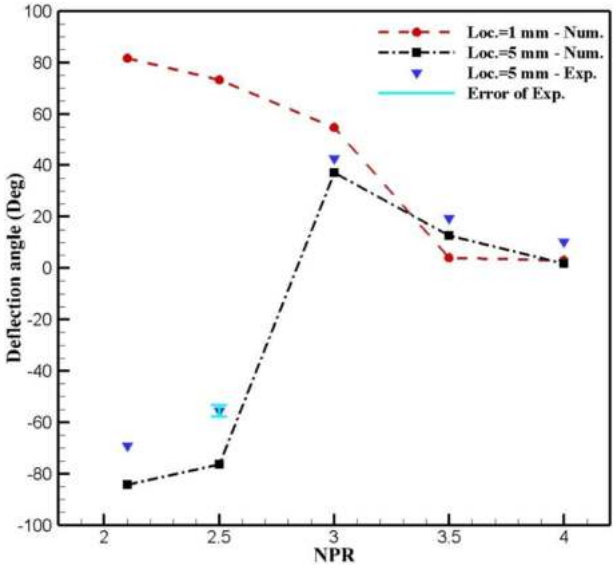

Fig. 20. The numerical and experimental amount of deviation of the thrust vector angle relative to the NPR for the different locations of the protuberance with the Pen. of 6%.

derive diverse parameters, elucidating the intricate details of the flow physics within this system. The variables under investigation encompass the protuberance's location, the protuberance penetration depth, and the nozzle pressure ratio (NPR). These variables are examined at distances of 1 and 5 mm from the throat, 2, 6, and 10 percent of throat height, and pressure ratios ranging from 2.1 to 4, respectively. Subsequent to this, a detailed discussion is provided regarding the outcomes of these considerations.

4.1. Investigating the effect of the presence of protuberance

As depicted in Fig. 14, the flow path of a sonic jet undergoes a notable transformation in its overall behavior and flow physics in the presence of a protuberance. The introduction of a protuberance into the sonic jet's flow instigates the development of shocks ahead of the flow, attributed to the abrupt pressure change within the flow. In this approach, manipulating shocks generated in a particular section of the nozzle has been attempted to control the thrust vector. Consequently, this technique is classified within the realm of shock control methods.

This method involves the placement of a protuberance near the nozzle outlet within the primary flow path. The presence of the protuberance in the main flow path induces the separation of the boundary layer from the wall, giving rise to shocks. Ultimately, these generated shocks instigate flow deviation. The primary cause of the formation of

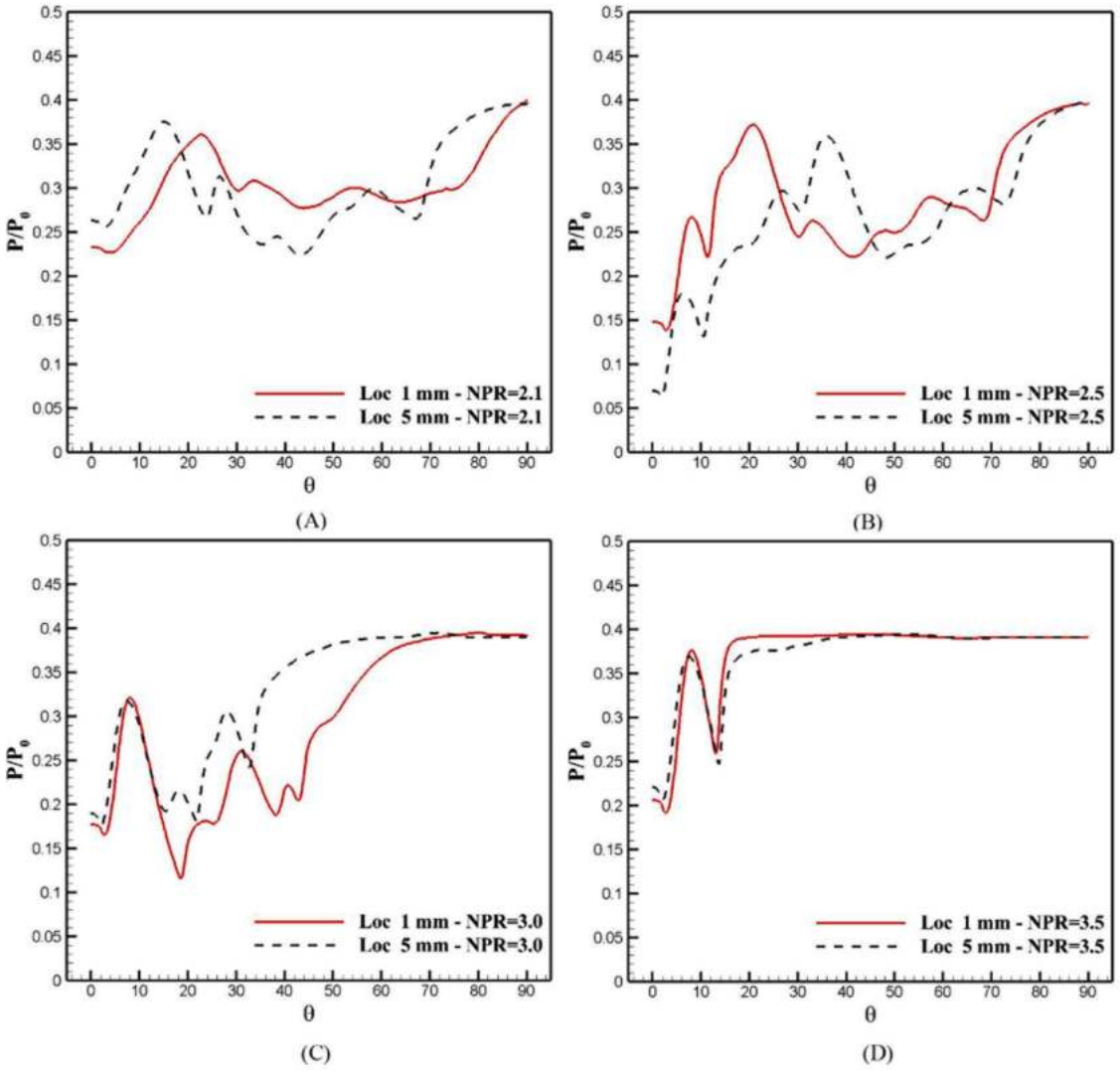

Fig. 21. Pressure distribution on the Coanda flap, which flow is attached, for different positions of the Pen. of 6%, NPR; (A) 2.1, (B) 2.5, (C) 3 & (D) 3.5.

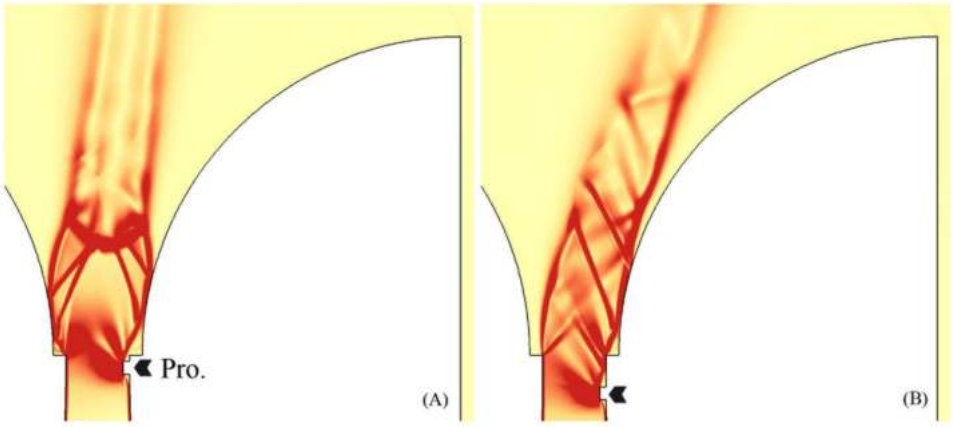

Fig. 22. Contour of density changes for the penetration depth of 10% at NPR=3.5, Loc.; (A) 1 mm & (B) 5 mm.

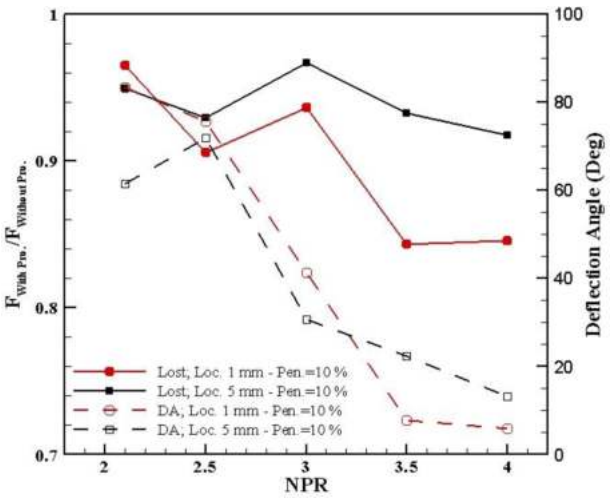

Fig. 23. The amount of force loss and the deviation of the thrust vector relative to the various NPRs for the location of 1 and 5 mm in Pen. of 10%.

these shocks, known as Lambda shocks and bow shocks, lies in the obstructive effects within the sonic flow and the distinctive nature of this flow. These shocks bring about a significant alteration in static pressure on the body. The modification in pressure on the body constitutes one of the factors contributing to the generation of lateral forces in the nozzle. However, the shock generated also induces a change in the flow angle, serving as a secondary factor in altering the thrust vector angle.

As previously mentioned, in this technique, the flow is deflected by the shock induced through the presence of the protuberance, and the Coanda effect is harnessed to sustain the flow on the flap, ultimately achieving high deflection angles. The operation of the Coanda effect in this system is delineated as follows: as the jet passes in proximity to the curved surface of the flap, the air situated between the jet mass and the flap wall either moves downward with the jet mass or becomes entrained within the jet mass. Consequently, the fluid confined between the jet and the wall experiences an increased velocity, leading to a reduction in pressure, while on the opposite side, there is no pressure reduction owing to the open atmosphere. This asymmetry in velocity profiles, arising from disparate pressures on both sides, generates a force exerted on the outer wall of the jet mass, deflecting the jet towards the wall and causing the fluid to adhere to the wall. These occurrences constitute the primary mechanism of the Coanda effect on the deflection vector of the thrust resulting from the nozzle flow. In Fig. 15, a combination of numerical simulations from the current study and schematic images illustrates various physical flow phenomena that arise due to the presence of a protuberance in a sonic flow and their impact on system performance.

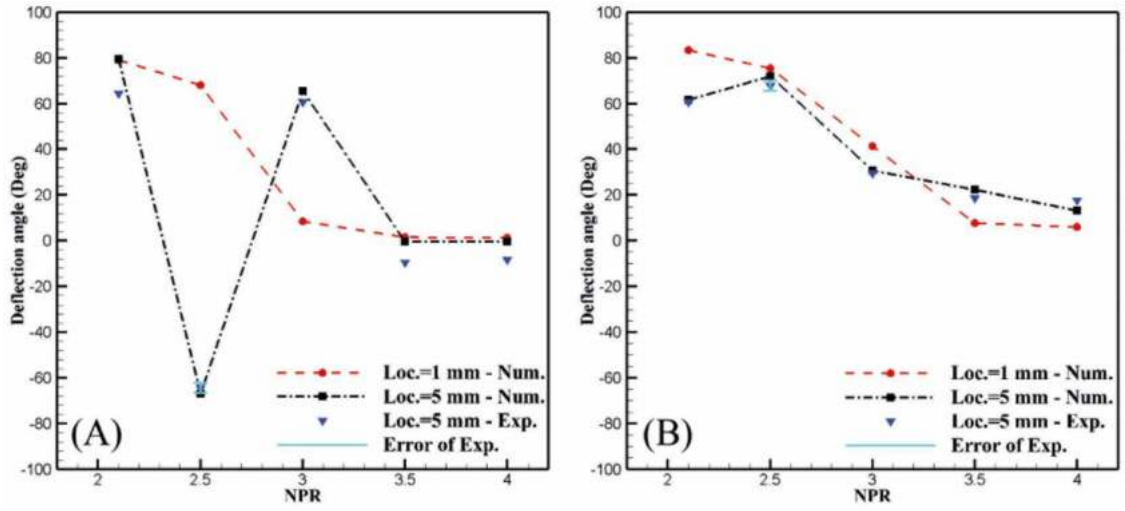

Fig. 24. The numerical and experimental amount of deviation of the thrust vector angle relative to the NPR for the different locations of the Pen. of; (A) 2% & (B) 10%.

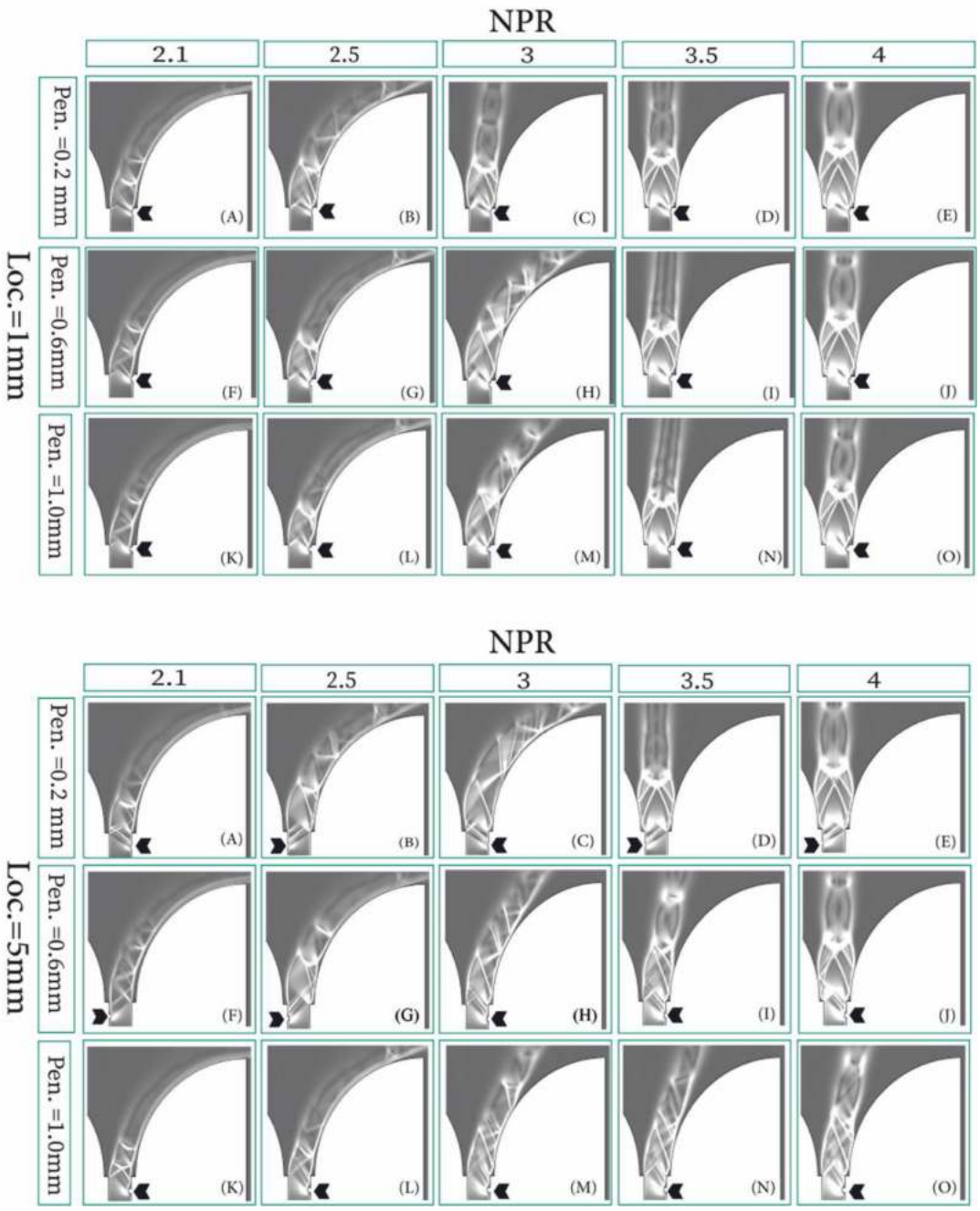

Fig. 25. Second differential images of density: comparison of placement location and penetration rate of protuberance in different pressure ratios.

4.2. The importance of nozzle pressure ratio

The flow physics for a position with the protuberance situated 1 mm from the throat and a penetration depth of 2 percent are illustrated in the Fig. 16 for two pressure ratios of 2.5 and 3. It is evident that, despite a 20 percent increase in the pressure ratio within the specified range, a significant transformation has occurred in the flow physics, leading to a dramatic change in the flow angle. Consequently, the nozzle pressure ratio can significantly influence the thrust vector in the discussed technique.

4.3. Investigating the effect of the location of the protuberance

In Figs. 17 and 18, contour plots illustrating density variations are observed for a penetration depth of 2 percent and, respectively, for pressure ratios of 2.5 and 3 at different protuberance locations. Although it can be observed that under these conditions, the behavior of the system for placement locations of 1 and 3.5 mm is very close to each other, from a general perspective, it is evident that the flow physics and thrust vector angle fundamentally depend on the protuberance location in these scenarios. At a pressure ratio of 3, at a location of 1 mm, the momentum loss appears to be less than that observed at a position located 5 mm away, resulting in the formation of a Mach disk. Meanwhile, the reflective effects of shocks on the opposite wall for the position located 5 mm cause a more intense energy loss, and oblique and reflected shocks are observed in this case. It is noteworthy that, as expected, the increase in momentum due to a rise in the pressure ratio leads to a strengthened Mach disk and reflective shocks, resulting in relatively more substantial jet plumes.

The sensitivity and dependence of the nozzle performance on the

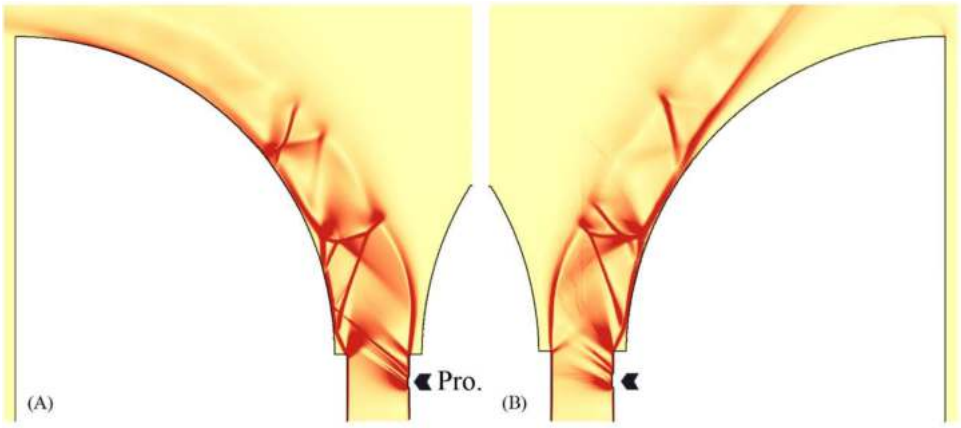

Fig. 26. Contour of density changes for the penetration depth of 2% at NPR=2.5 and Loc. 3.5 mm; (A) 1.5 mm & (B) 2 mm.

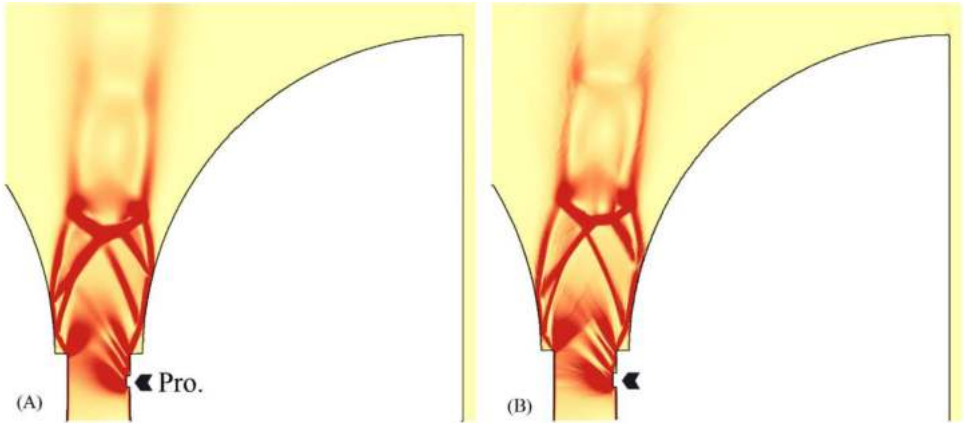

Fig. 27. Contour of density changes for the penetration depth of 6% at NPR=3.5 and Loc. 3.5 mm; (A) 1.5 mm & (B) 2 mm.

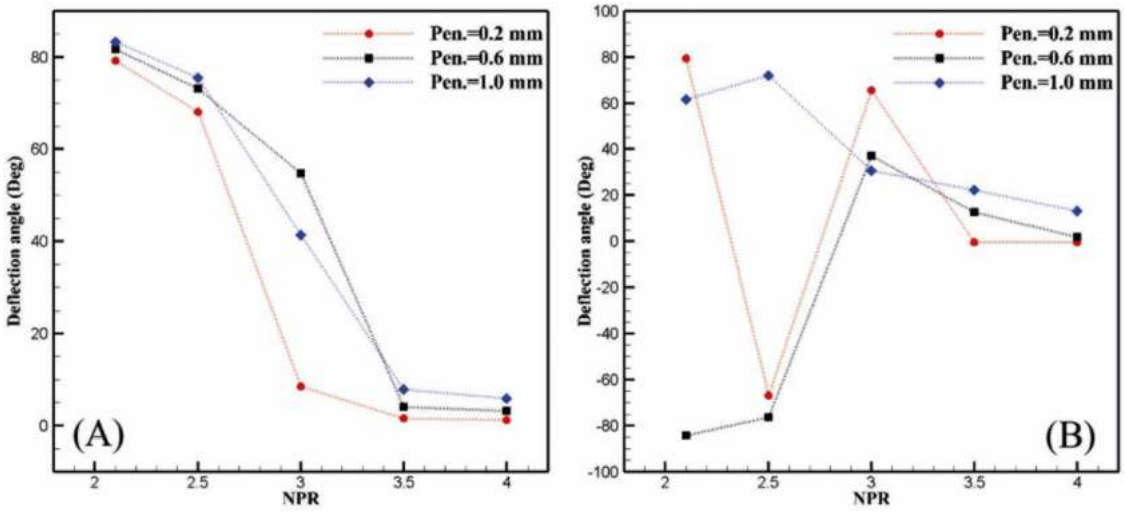

Fig. 28. The amount of deviation of the thrust vector angle relative to the NPR for the different depth of penetration of the protuberance, Loc.; (A) 1 mm & (B) 5 mm.

nozzle pressure ratio and protuberance location are not exclusive to a penetration depth of 2 percent. The significance of the pressure ratio and placement is also evident in the Fig. 19 for a penetration depth of 6 percent.

As depicted in Fig. 20, at a penetration depth of six percent, the nozzle pressure ratio and protuberance location influence the system behavior concerning the magnitude and direction of flow deflection. In this scenario, the direction of deflection is primarily determined by the protuberance location for pressure ratios less than three. However, the protuberance location does not exclusively dictate the maximum deflection magnitude. With an escalation in the pressure ratio, this reliance on the protuberance location diminishes, and the deflection

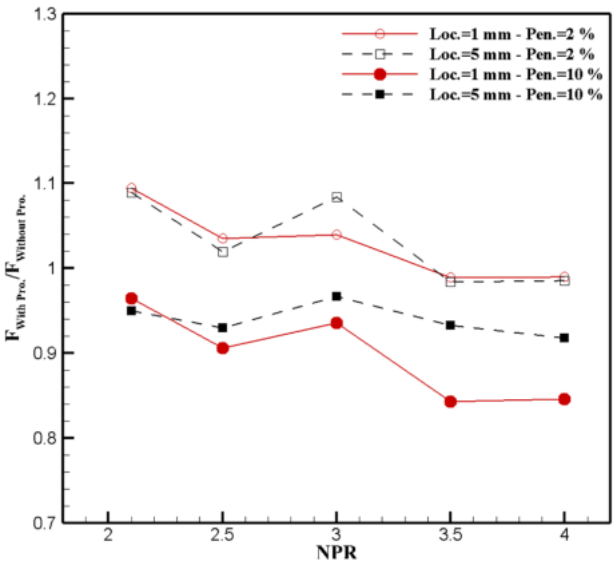

Fig. 29. Comparison of the amount of force loss relative to the various NPRs for the different depths of penetration of 2 and 10% and for the Loc. 1 mm and 5 mm.

magnitude gradually decreases, becoming solely contingent on the pressure ratio.

In Fig. 21, the pressure distribution on the Coanda flap, towards which the flow has been deflected, is depicted for a protuberance with a penetration depth of 6 percent at two positions, 1 and 5 mm from the nozzle outlet. The placement of shocks and, consequently, the point of flow separation from the flap is influenced by the protuberance location across a broad range of pressure ratios examined. However, at a pressure ratio of 3.5, this behavior becomes independent of the protuberance location, and beyond that point, the flow gradually separates from the flap at a nearly similar position.

Therefore, for pressure ratios exceeding 3, the system's behavior in terms of thrust vector deflection becomes nearly independent of the protuberance location. Notably, as illustrated in Fig. 19, although the separation point is proximate for the two protuberance locations at a pressure ratio of 3.5, the flow physics for these instances differ significantly. At the 1-mm protuberance location, the jet plume exhibits greater expansiveness, and a more robust Mach disk forms, while at the 5-mm protuberance location, more oblique and reflective shocks are observed.

Fig. 22 also depicts the flow physics for two distinct protuberance locations with a penetration depth of 10 percent at a pressure ratio of 3.5. Similar to the aforementioned cases, the impact of the protuberance location on the flow physics is observable at this penetration depth.

Considering Fig. 23, as expected from the aforementioned flow physics, in the case of a protuberance located 1 mm from the throat, a significantly higher thrust loss is observed compared to the 5-mm protuberance location due to the formation of the Mach disk. Notably, this difference becomes more pronounced with an increase in the pressure ratio and the strengthening of the Mach disk. Another point, as depicted in Figs. 25 and 30, is that no Mach disk is formed at a pressure ratio of 2.1, and weak shocks are observed, resulting in lower thrust loss. The reason why the thrust loss in the 5-mm protuberance location is more significant than in other locations at this pressure ratio could be attributed to the shock impacting the opposite wall and causing more energy loss. However, with an increase in the pressure ratio and, consequently, the momentum of the flow, leading to the formation of the Mach disk, the trend of thrust loss undergoes a complete change. Another noteworthy observation is that, for the 5-mm protuberance location (images k to o in Fig. 30) and at all pressure ratios, the energy loss due to flow blockage by the protuberance and the reflection of shocks against the opposite wall of the protuberance has been so severe that it has significantly influenced the trend of shock formation. This energy loss in the fluid flow has led to a substantial loss of momentum, resulting in much weaker shocks than under corresponding conditions. This phenomenon could be a reason for the absence of Mach disk formation even at a pressure ratio of 4 in this configuration.

In Fig. 24, the deflection angle of the jet for various NPRs is displayed for protuberances with penetration depths of 2 and 10 percent, located at positions 1 and 5 mm from the throat. Notably, the 5-mm position has also been experimentally reported to validate the accuracy of numerical simulation results and ensure confidence in the associated processes. The results in Fig. 24-a indicate that for a protuberance located 5 mm from the throat, increasing NPR from 2.1 to 2.5 induces a significant change in the jet vector's deflection angle, decreasing from approximately 80° to around 70°. Furthermore, with a further increase in NPR up to 3, the deflection angle of the jet returns to about 70°, indicating that the flow has generally shifted from one side of the nozzle to the other. However, as expected, with increasing NPR, due to the increase in momentum, the degree of flow deflection decreases, and for NPRs of 3.5 and above, only a very slight deflection is observed. This is in contrast to the same plot for the protuberance located 1 mm from the throat nozzle, as illustrated in Fig. 25. As seen in the figure, the flow in the entire range of discussed pressure ratios deflects toward the nozzle (the same side as the protuberance location), and with an increase in NPR, the degree of flow deflection decreases more steadily compared to the 5-mm position, reducing from 80° to approximately five degrees. Consequently, in the case of the 1-mm protuberance location, the system's behavior concerning pressure ratio changes has been more stable. Another point to note is that a significant difference in the deflection magnitude is observed in the 5-mm protuberance location and at NPR 3. The reason for this can be demonstrated in the numerical contour plots shown in image c of Fig. 25. As evident, at a penetration depth of 2 percent, the shock effect and its collision with the wall cause flow deflection in the 5-mm position, while in the 1-mm position, the shock does not collide with the wall, resulting in the flow not deviating to the Coanda flap.

Fig. 24-B illustrates that increasing the protuberance penetration depth up to ten percent of the throat height results in the stability of the system's behavior across the entire range of discussed pressure ratios. This implies that the deflection direction and magnitude of the flow are nearly independent of the protuberance location. According to Fig. 25, the shock angle formed in this situation, upon the collision of the flow with the protuberance, is such that it does not hit the opposite wall. Similar to a penetration depth of six percent, in this case, for the protuberance located 1 mm away, a Mach disk is formed for pressure ratios of 3.5 and 4. In contrast, for the 5-mm location, due to shock angles, no Mach disk is formed. As shown in Fig. 23, the effect of forming these Mach disks on the significant thrust reduction is evident.

The conclusion drawn from the comprehensive analyses is that the system's behavior in controlling the thrust vector, encompassing both the direction and magnitude of the jet vector deflection, is contingent upon the protuberance's penetration depth, in addition to its location. Consequently, it is not feasible to analyze the effect of the protuberance's location without considering its penetration depth.

4.4. Investigation of the width of the protuberance

The flow physics for a position with the protuberance situated 3.5 mm from the throat and a penetration depth of 2 percent under NPR=2.5 are illustrated in the Fig. 26 for two protuberance widths of 1.5 and 2 mm . It is evident that, despite a very small change in the width of the protuberance, a significant transformation has occurred in the flow physics, leading to a dramatic change in the flow angle. Consequently, the width of the protuberance can significantly influence the thrust vector in the discussed technique, as it can determine the first point of encounter of the jet front with the protuberance. Thus, from some perspectives, it is a parameter similar to the location of the protuberance.

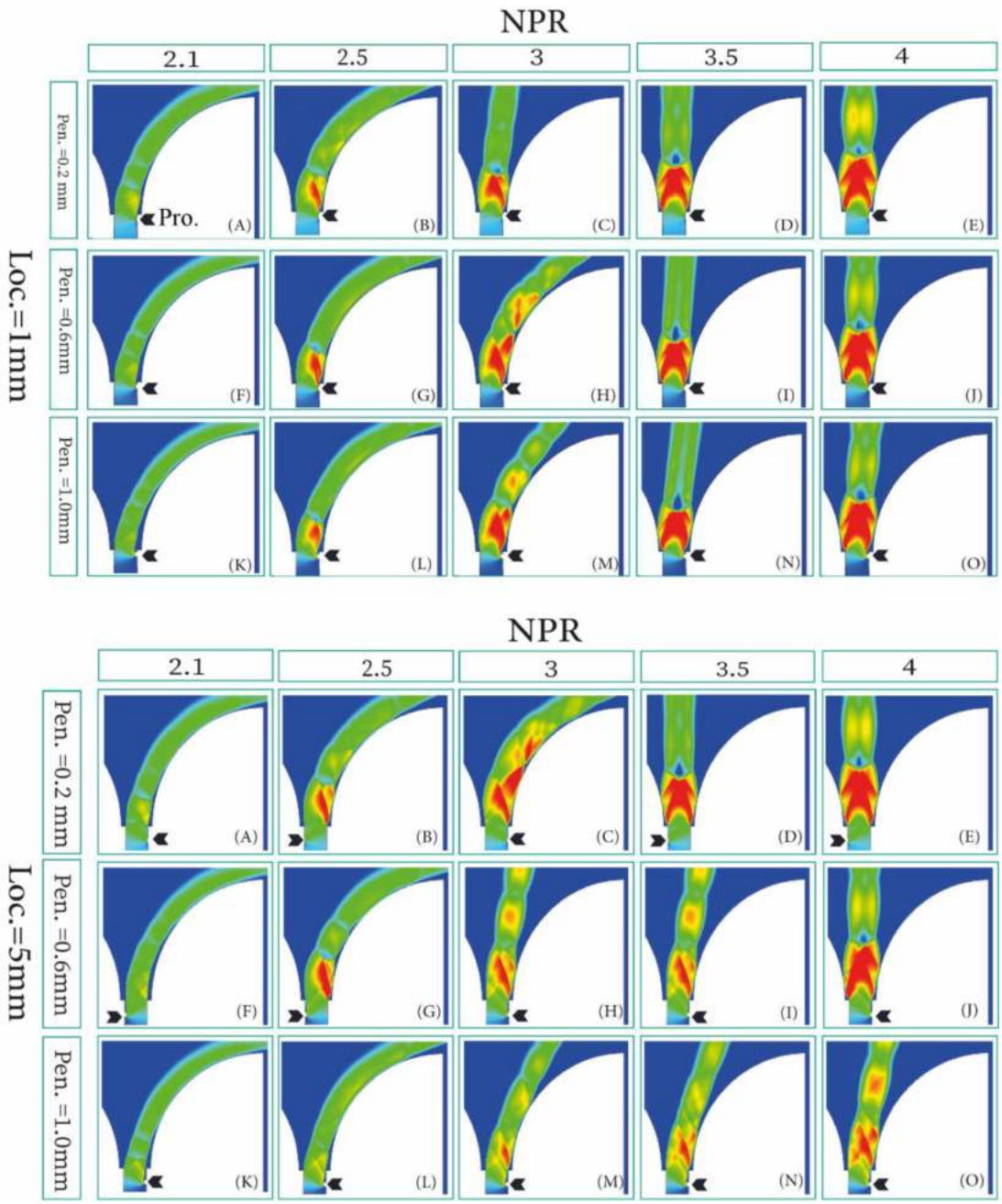

Fig. 30. Mach contours: comparison of placement location and penetration rate of protuberance in different pressure ratios.

Subsequently, the influence of protuberance width on nozzle behavior was investigated for penetration of 6% under NPR=3.5, as depicted in the Fig. 27. It was observed that similar to the location of the protuberance, the behavior became independent of protuberance width with increasing pressure ratio and blockage effects caused by the protuberance. This suggests a dominant influence of shock strength on nozzle behavior, overriding the impact of protuberance width.

4.5. Investigation of the penetration depth of the protuberance

As demonstrated and evident in the overall trend of the Fig. 28, the flow deviation behavior based on the protuberance's penetration depth is entirely contingent on the protuberance's location for different NPRs. The trend of changes in this behavior concerning the penetration depth for the protuberance placed 1 mm away from the nozzle's throat remains generally uniform and stable within the examined pressure ratios. However, it significantly differs for the protuberance set 5 mm away from the nozzle outlet, especially for pressure ratios less than 3.5. Given that the presence of protuberance is the primary factor in the formation and determination of the strength of shocks, it is expected that the flow deviation of the jet increases with an increase in penetration depth and, consequently, its obstructive effects. However, as the graphs indicate, this expectation is not met at all examined points. For instance, an exception to this trend can be observed at a pressure ratio of 3. In this pressure ratio, for penetration depths of 6 and 10 percent at the location 1 mm away from the throat and for all examined penetration depths at the location of 5 mm , an increase in penetration depth results in a lesser deviation in the jet. The cause of this phenomenon can be illustrated in the contour plots of the Mach number depicted in Fig. 30, representing the flow physics. As observed, the size of the jet plumes significantly impacts the attachment, or in other words, the point of flow separation from the Coanda flap. Therefore, it seems that changing the radius or

distance of the Coanda flap from the nozzle exit can influence the point of separation. The extent of the effect of these parameters, in turn, can be subject to investigation in future studies.

Another notable observation is the attainment of an angle of deviation of approximately 20° for the protuberance situated 5 mm away from the nozzle throat with a penetration depth of 10 percent at a pressure ratio of 4. This level of deflection for a sonic jet under this pressure ratio holds considerable significance compared to alternative strategies for thrust vectoring and, indeed, other configurations investigated within the framework of the technique presented in this article.

In Fig. 29, it is evident that the increased blockage effects of the protuberance with a higher penetration depth result in a more pronounced thrust loss for the protuberance with a penetration depth of 10 percent compared to the protuberance with a penetration depth of 2 percent in both protuberance positions. This difference averages approximately ten to fifteen percent. The change in thrust due to the presence of the protuberance with a penetration depth of 2 percent is almost negligible, and it is not significantly influenced by the protuberance's placement, except at a pressure ratio of three, where the flow in the 5-mm protuberance position is completely deflected due to the shock impacting the opposite wall. In contrast, in the 1-mm protuberance position, a shock is formed without affecting the opposite wall, exiting from the nozzle throat and causing an overall flow deflection. However, for a penetration depth of 10 percent, the placement of the protuberance significantly affects the thrust loss. In this case, due to the absence of a Mach disk at the 5-mm protuberance position, we observe a lower thrust loss than the 1-mm protuberance position. Remarkably, in the 5-mm protuberance position with a penetration depth of 10 percent, the thrust loss appears to be nearly independent of the nozzle pressure ratio, unlike other conditions that exhibit nonlinear behavior.

By comparing these conditions, it can be asserted that the penetration depth and the placement of the protuberance significantly influence the maximum deviation angle. Within this system, where the protuberance and the Coanda effect are employed, a maximum deviation angle of 83° has been attained for sonic flow. Nevertheless, the direction and magnitude of flow deviation are profoundly impacted by the penetration depth and protuberance placement in relation to different nozzle pressure ratios (NPRs), leading to a substantial variation in the system's behavior based on these factors.

Fig. 30 illustrates the Mach number contour for this study's investigated conditions, offering a comprehensive overview of the results. This facilitates a comparative analysis of the system's behavior and performance across various scenarios.

5. Conclusion

This study has investigated a novel and effective technique for sonic jet control that combines a protuberance with the Coanda effect. The findings demonstrate that this approach achieves remarkable thrust vector deflection angles, with a maximum of 83° being reached. Notably, at a pressure ratio of 4, a 20-degree deflection can be achieved by a protuberance that is placed at the location of 5 mm from the throat with a 10% penetration depth, surpassing the performance of other control methods.

Several key factors influencing the system's behavior were identified through the research. The protuberance location significantly impacts shockwave formation and flow separation, leading to variations in thrust loss and jet plume characteristics. The penetration depth also plays a crucial role, affecting flow deviation behavior in relation to pressure ratio. More stable system behavior across various pressure ratios was observed with a deeper penetration depth (10%) compared to shallower depths (2%).

While the maximum achievable deviation angle appears independent of protuberance location and penetration depth, these factors significantly influence the direction and magnitude of deviation at different pressure ratios. This highlights the complex interplay between these parameters and underscores the need for further investigation.

Future research should aim to explore the system's stability and performance in more detail. This could involve quantitative evaluation under varying Coanda flap configurations and the utilization of multiple protuberances tailored to specific pressure ratios. The optimization of these parameters holds promise for further enhancing the effectiveness and controllability of this innovative sonic jet thrust vectoring technique.

CRediT authorship contribution statement

Mohammad Reza Soufivand: Writing – original draft, Validation, Investigation. **Mohammad Hojaji:** Writing – review & editing, Supervision, Project administration, Investigation. **Mohammad Hossein Razavi Dehkordi:** Writing – review & editing, Investigation.

Declaration of competing interest

The authors declare the following financial interests/personal relationships which may be considered as potential competing interests:

I want to emphasize that Islamic Azad University is an independent and private academic institution, unaffiliated with any government or government entity. The research work I conducted there was solely an academic endeavor, funded privately without any industrial involvement. If there are other authors, they declare that they have no known competing financial interests or personal relationships that could have appeared to influence the work reported in this paper.

Data availability

Data will be made available on request.

References

[1] Sutton GP, Biblarz O. Rocket propulsion elements john. New York: WILEY & SONS. Inc; 2001.
[2] Wu K, Kim TH, Kim HD. Theoretical and numerical analyses of aerodynamic characteristics on shock vector control. J Aerosp Eng 2020;33(5):04020050.
[3] Chouicha R, Sellam M, Bergheul S. Effect of reacting gas on the fluidic thrust vectoring of an axisymmetric nozzle. Propuls Power Res 2020.
[4] Hakim K, Toufik H, Said B. Numerical simulation of fluidic thrust vectoring in the conical nozzle. J Adv Res Fluid Mech Therm Sci 2020;73(2):88–105.
[5] Wu K, Kim T, Kim H. Sensitivity analysis of counterflow thrust vector control with a three-dimensional rectangular nozzle. J Aerosp Eng 2021;34(1):04020107.
[6] Wu K, Kim T, Kim H. Numerical study of fluidic thrust vector control using dual throat nozzle. J Appl Fluid Mech 2020;14(1):73–87.
[7] Hojaji M, Razavi Dehkordi MH, et al. Experimental study of the effects of secondary flow injection on the exhaust flow of converging-diverging nozzles at different oblique angles. Aeronautic Eng 2022;24(1):45–56.
[8] Lin W, Shi Q, Liu S, Lin Z, Tong Y, Su L, et al. Study of thrust vector control for the rotating detonation model engine. Int J Hydrogen Energy 2022;47(2):1292–305.
[9] Rose DBB, Sridhar B. A rectangular strut on the expansion ramp of a scramjet thruster for thrust vector control. Acta Astronaut 2022;194:9–21.
[10] Xia H, Wang P, Dong H, Jin Z, An X, Fang L. Hydrodynamic characteristics of a new thrust vectoring ducted propeller with slotted nozzle. Ocean Eng 2022;266:112805.
[11] Wu K. Study on aerodynamic features of rod thrust vector control for physical applications. Proc Inst Mech Eng Part G J Aerosp Eng 2023;237(1):156–76.
[12] Afridi S, Khan TA, Shah SIA, Shams TA, Mohiuddin K, Kukulka DJ. Techniques of fluidic thrust vectoring in jet engine nozzles: a review. Energies. 2023;16(15):5721.
[13] Deere K. editor Summary of fluidic thrust vectoring research at NASA Langley Research Center. In: 21st AIAA applied aerodynamics conference; 2003.
[14] Páscoa JC, Dumas A, Trancossi M, Stewart P, Vucinic D. A review of thrust-vectoring in support of a V/STOL non-moving mechanical propulsion system. Central Eur J Eng 2013;3:374–88.
[15] Tahani M, Hojaji M, Mahmoodi Jezeh SV. Turbulent jet in crossflow analysis with LES approach. Aircraft Eng Aerospace Technol 2016;88(6):717–28.
[16] Hojaji M, Soltani M, Taeibi-Rahni M. New visions in experimental investigations of a supersonic under-expanded jet into a high subsonic crossflow. Proc Inst Mech Eng Part G J Aerosp Eng 2010;224(10):1069–80.
[17] Viti V, Neel R, Schetz JA. Detailed flow physics of the supersonic jet interaction flow field. Phys Fluids 2009;21(4):046101.

[18] Santiago JG, Dutton JC. Crossflow vortices of a jet injected into a supersonic crossflow. AIAA J 1997;35(5):915–7.
[19] Strykowski PJ, Krothapalli A, Forliti D. Counterflow thrust vectoring of supersonic jets. AIAA J 1996;34(11):2306–14.
[20] Flamm J. Experimental study of a nozzle using fluidic counterflow for thrust vectoring. In: 34th AIAA/ASME/SAE/ASEE Joint Propulsion Conference and Exhibit; 1998.
[21] Alvi F, Strykowski P. Forward flight effects on counterflow thrust vector control of a supersonic jet. AIAA J 1999;37(2):279–81.
[22] Wing DJ. Static investigation of two fluidic thrust-vectoring concepts on a two-dimensional convergent-divergent nozzle: national aeronautics and space administration. Langley Research Center; 1994.
[23] Mason M, Crowther W. Fluidic thrust vectoring for low observable air vehicles. In: 2nd AIAA flow control conference; 2004.
[24] Banazadeh A, Saghafi F, Ghoreyshi M, Pilidis P. Experimental and computational investigation into the use of co-flow fluidic thrust vectoring on a small gas turbine. The Aeronautical Journal 2008;112(1127):17–25.
[25] Song M, Park S, Lee Y. Application of backstep Coanda flap for supersonic coflowing fluidic thrust-vector control. AIAA J 2014;52(10):2355–9.
[26] Bettridge MW, Smith BL, Spall RE. Aerodynamic jet steering using steady blowing and suction. Exp Fluids 2006;40(5):776–85.
[27] Forster MJ. Computational modelling of transonic circulation control: the university of liverpool (United kingdom). 2017.
[28] Matsuo S, Setoguchi T, Kudo T, Yu S. Study on the characteristics of supersonic Coanda jet. J Therm Sci 1998;7:165–75.
[29] Warsop C. Thrust vectoring apparatus for a jet engine, corresponding jet engine, thrust vectoring method and upgrading method for a jet engine. Google Patents; 2014.
[30] Lee Y, Park S, Kim Y. Thrust vectoring of sonic jet by using coanda flap and solenoid valve. AIAA J 2016;54(9):2909–15.
[31] Lee M, Song M, Kim D, Lee Y. Bidirectional Thrust Vectoring Control of a Rectangular Sonic Jet. AIAA J 2018;56(6):2494–8.
[32] Noaman H, Tang HB, Khalil E. Numerical Simulation on the Influence of Injection Location, Injection Angle, and Divergence Half Angle on SITVC Nozzle Flow Field. Int J Aerospace Eng 2019. 2019.
[33] Li L, Hirota M, Ouchi K, Saito T. Evaluation of fluidic thrust vectoring nozzle via thrust pitching angle and thrust pitching moment. Shock Waves 2017;27(1):53–61.
[34] Salehifar M, Tahani M, Hojaji M, Dartoomian A. CFD modeling for flow field characterization and performance analysis of HGITVC. Appl Therm Eng 2016;103:291–304.